A Compressible Nonhydrostatic Cell-Integrated Semi-Lagrangian Semi-Implicit Solver (CSLAM-NH) with Consistent and Conservative Transport

MAY WONG

University of British Columbia, Vancouver, British Columbia, Canada

WILLIAM C. SKAMAROCK, PETER H. LAURITZEN, AND JOSEPH B. KLEMP

National Center for Atmospheric Research, Boulder, Colorado*

ROLAND B. STULL

University of British Columbia, Vancouver, British Columbia, Canada

(Manuscript received 27 June 2013, in final form 26 September 2013)

ABSTRACT

A cell-integrated semi-Lagrangian (CISL) semi-implicit nonhydrostatic solver for the fully compressible moist Euler equations in two-dimensional Cartesian (*x*–*z*) geometry is presented. The semi-implicit CISL solver uses the inherently conservative semi-Lagrangian multitracer transport scheme (CSLAM) and a new flux-form semi-implicit formulation of the continuity equation that ensures numerically consistent transport. The flux-form semi-implicit formulation is based on a recent successful approach in a shallow-water equations (SWE) solver (CSLAM-SW). With the new approach, the CISL semi-implicit nonhydrostatic solver (CSLAM-NH) is able to ensure conservative and consistent transport by avoiding the need for a time-independent mean reference state. Like its SWE counterpart, the nonhydrostatic solver presented here is designed to be similar to typical semi-Lagrangian semi-implicit schemes, such that only a single linear Helmholtz equation solution and a single call to CSLAM are required per time step. To demonstrate its stability and accuracy, the solver is applied to a set of three idealized test cases: a density current (dry), a gravity wave (dry), and a squall line (moist). A fourth test case shows that shape preservation of passive tracers is ensured by coupling the semi-implicit CISL formulation with existing shape-preserving filters. Results show that CSLAM-NH solutions compare well with other existing solvers for the three test cases, and that it is shape preserving.

1. Introduction

Semi-Lagrangian semi-implicit (SLSI) schemes have been widely used in climate and numerical weather prediction (NWP) models since the pioneering work of Robert (1981) and Robert et al. (1985). The more lenient numerical stability condition in these schemes allows larger time steps and thus increased computational efficiency. Traditional semi-Lagrangian schemes are not inherently mass conserving because of their use of gridpoint interpolation, and the lack of conservation can lead to accumulation of significant solution errors (Rasch and Williamson 1990; Machenhauer and Olk 1997). To address this issue, conservative semi-Lagrangian schemes, also called cell-integrated semi-Lagrangian (CISL) transport schemes (Rancic 1992; Laprise and Plante 1995; Machenhauer and Olk 1997; Zerroukat et al. 2002; Nair and Machenhauer 2002; Lauritzen et al. 2010), have been developed. Although CISL transport schemes, when applied in fluid flow solvers, allow for locally (and thus globally) conservative transport of total fluid mass and constituent (i.e., tracer) mass, a lack of consistency arises between the numerical representation of the total dry air mass conservation, to which we will refer as the

---

* The National Center for Atmospheric Research is sponsored by the National Science Foundation.

Corresponding author address: May Wong, Dept. of Earth, Ocean, and Atmospheric Sciences, University of British Columbia, 2020-2207 Main Mall, Vancouver, BC V6T 1Z4, Canada.
E-mail: mwong@eos.ubc.ca

DOI: 10.1175/MWR-D-13-00210.1

continuity equation, and constituent mass conservation equations (Jöckel et al. 2001; Zhang et al. 2008; Wong et al. 2013). Numerical consistency in the flux-form equation for a tracer requires the equation for a constant tracer field to correspond numerically to the mass continuity equation; this consistency ensures that an initially spatially uniform passive tracer field will remain so. The lack of numerical consistency between the two can lead to the unphysical generation or removal of model constituent mass, which can introduce significant errors in applications such as chemical tracer transport (Machenhauer et al. 2009).

Recently, Wong et al. (2013) introduced a new flux-form formulation of the semi-implicit CISL height conservation equation for the shallow-water equations (SWE) solver. They showed that the scheme is accurate and stable even for highly nonlinear barotropically unstable jets and large Courant numbers. They also found that the use of a shape-preserving filter in an inconsistent formulation of the continuity equations is ineffective, highlighting the importance of numerical consistency in these models.

In this paper, the flux-form semi-implicit SWE formulation is extended to the fully compressible two-dimensional (x–z) moist nonhydrostatic equations for the atmosphere. A nonhydrostatic model permits fast-moving internal gravity and acoustic waves. Here, we integrate the terms responsible for the acoustic waves in a semi-implicit manner to allow large time steps while maintaining stability for these waves. As in Wong et al. (2013), our nonhydrostatic solver is based on CSLAM, a CISL transport scheme developed by Lauritzen et al. (2010) that has been implemented in the National Center for Atmospheric Research (NCAR) High-Order Methods Modeling Environment (HOMME; Erath et al. 2012). We refer to this new conservative and consistent nonhydrostatic solver that uses CSLAM for transport as CSLAM-NH.

The semi-implicit CISL nonhydrostatic solver has six main advantages and desirable properties. As we will show, our nonhydrostatic cell-integrated semi-Lagrangian solver is 1) inherently mass conserving, 2) shape preserving, and, with the new formulation, 3) has numerically consistent transport. 4) The discretization does not depend on a mean reference state, but maintains the same framework as typical semi-implicit CISL solvers, where 5) a single linear Helmholtz equation is solved and 6) a single application of CSLAM is needed per time step.

The paper is organized as follows. The governing equations of the two-dimensional fully compressible nonhydrostatic system are first described in section 2. We then present the proposed discretization of the governing equations, including a consistent formulation of the moisture conservation equations (section 3). The desirable properties of the nonhydrostatic solver are discussed in section 4. We test the nonhydrostatic solver with three idealized test cases and compare results with an Eulerian split-explicit time-stepping scheme (section 5). A fourth test case on numerical consistency is also presented in section 5 to demonstrate the shape-preserving ability of the solver with additional passive tracers. A summary is given in section 6.

2. Governing equations

The model governing equations are the two-dimensional (x–z) moist Euler equations in Cartesian geometry:

$$\frac{\partial u}{\partial t} + u\frac{\partial u}{\partial x} + w\frac{\partial u}{\partial z} = -\frac{\pi}{\rho_m}\gamma R_d\frac{\partial \Theta'_m}{\partial x} + F_u, \tag{1}$$

$$\frac{\partial w}{\partial t} + u\frac{\partial w}{\partial x} + w\frac{\partial w}{\partial z} = -\frac{\pi}{\rho_m}\gamma R_d\frac{\partial \Theta'_m}{\partial z} + \frac{g}{\rho_m}\left(\overline{\rho}_d\frac{\pi'}{\overline{\pi}} - \rho'_m\right) + F_w, \tag{2}$$

$$\frac{\partial \Theta_m}{\partial t} + \nabla\cdot(\Theta_m\mathbf{v}) = F_\Theta, \tag{3}$$

$$\frac{\partial \rho_d}{\partial t} + \nabla\cdot(\rho_d\mathbf{v}) = 0, \tag{4}$$

$$\frac{\partial Q_j}{\partial t} + \nabla\cdot(Q_j\mathbf{v}) = F_{Q_j}, \tag{5}$$

$$p = p_0\left(\frac{R_d\Theta_m}{p_0}\right)^\gamma, \tag{6}$$

where $\pi = (p/p_0)^\kappa$ is the Exner function, $\kappa = R_d/c_p$, $\gamma = c_p/c_v = 1.4$, $R_d = 287\,\mathrm{J\,kg^{-1}\,K^{-1}}$, $c_p = 1003\,\mathrm{J\,kg^{-1}\,K^{-1}}$, and $g = 9.81\,\mathrm{m\,s^{-2}}$. Perturbation variables from a time-independent hydrostatically balanced background state are used to reduce numerical errors in the calculations of the pressure gradient terms (Klemp et al. 2007). The hydrostatically balanced background state is defined as $d\overline{p}(z)/dz = -\overline{\rho}_d(z)g$. Perturbation variables are defined as $\Theta_m = \overline{\rho}_d(z)\overline{\theta}(z) + \Theta'_m$, $\pi = \overline{\pi} + \pi'$, $\rho_d = \overline{\rho}_d(z) + \rho'_d$, and the moist density $\rho_m = \rho_d(1 + q_v + q_c + q_r)$, where q_v, q_c, and q_r are the mixing ratios for water vapor, cloud, and rainwater, respectively. The $F_{(\cdot)}$ terms represent diffusion, and any diabatic effects and parameterized physics when moisture is present.

As in Klemp et al. (2007), fluxes are coupled to the dry density ρ_d. The flux variables are given as

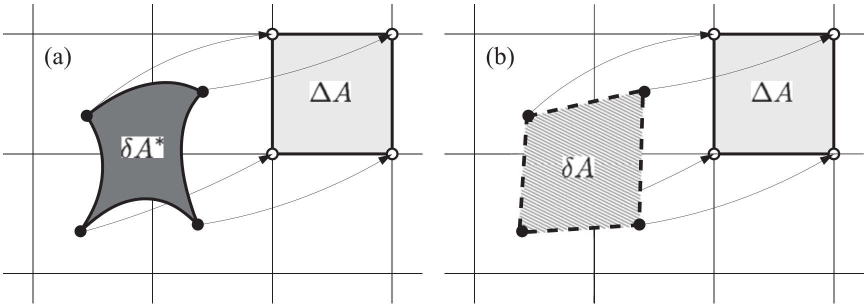

FIG. 1. (a) Exact departure cell area (δA^*, dark gray region) and the corresponding arrival grid cell (ΔA, light gray region). (b) Departure cells in CSLAM (δA) are represented as polygons defined by the departure locations of the arrival gridcell vertices (Wong et al. 2013).

$$\Theta_m = \rho_d \theta_m \quad \text{and} \quad Q_j = \rho_d q_j,$$

where θ_m is the modified potential temperature $\theta_m = \theta(1 + a'q_v)$, where $a' \equiv R_v/R_d \simeq 1.61$ and $q_j = (q_v, q_c, q_r)$.

The momentum equations are cast in their advective form, and all other equations (i.e., for density, potential temperature, and moist species) are cast in their conservative flux form. Pressure is a diagnostic variable given by the equation of state. The governing equations are based on Klemp et al. (2007); the pressure gradient terms in Eqs. (1) and (2) have been recast in terms of Θ'_m using Eq. (6) to derive the relation

$$\nabla p = \gamma R_d \pi \nabla \Theta_m,$$

which enables us to form an implicit equation for Θ' (section 3). The equations are still exact and no approximations have been applied. The only difference from the governing equations in Klemp et al. (2007) is that their momentum equations are cast in the conservative flux form, whereas the advective form is used here to facilitate the use of the traditional semi-Lagrangian method.

3. A consistent and mass-conserving nonhydrostatic solver

a. CSLAM—A conservative transport scheme

To ensure mass conservation, we utilize the inherently conservative semi-Lagrangian multitracer transport scheme (CSLAM; Lauritzen et al. 2010). The CSLAM is a backward-in-time CISL scheme,[1] where the departure grid cell area δA^* is found by tracing the regular arrival gridcell area ΔA back in time one time step Δt (Fig. 1a). The CSLAM discretization scheme for the lhs of Eqs. (3), (4), and (5) is given by

$$\phi^{n+1}_{\text{exp}} \Delta A = \int_{\delta A^*} \phi^n \, dA = \phi^n_* \delta A^*,$$

where $\phi = \Theta_m$, ρ_d, or Q_j. The superscript denotes the time level, and ϕ^{n+1}_{exp} is the explicit cell-averaged transport term computed by integrating the field ϕ^n over the departure cell area δA^*, which gives the cell-averaged departure value ϕ^n_*.

The departure cell area δA^* in CSLAM is found through iterative trajectory computations from the four vertices of an arrival grid cell (unfilled circles in Fig. 1b) to their departure points (filled circles in Fig. 1b). The departure cell area is then approximated using straight lines as cell edges[2] (dark gray region δA in Fig. 1b). To integrate the field ϕ^n over δA, CSLAM implements a remapping algorithm that consists of a piecewise quasi-biparabolic subgridcell reconstruction of ϕ^n in the two coordinates as in Nair and Machenhauer (2002) with an additional cross term as described in Jablonowski (2004) that helps smooth subgrid distribution near sharp gradients:

$$\phi^n(x,z) = \langle \phi^n \rangle + a^x x + b^x \left(\frac{1}{12} - x^2\right) + a^z z + b^z \left(\frac{1}{12} - z^2\right) + \frac{1}{2}(c^{xz} + c^{zx})xz, \qquad (7)$$

where coefficients a^x, b^x, a^z, and b^z of the reconstructed parabolic function in the two coordinates are obtained as in Nair and Machenhauer (2002), and the cross-term coefficients c^{xz} and c^{zx} are obtained as in Jablonowski (2004). An average of the two coefficients of the cross term, c^{xz} and c^{zx}, is taken to avoid a directional bias (Jablonowski 2004). The cell-average value over the Eulerian grid cell is denoted as $\langle \phi^n \rangle$.

---

[1] Note that CSLAM may also be cast in flux form (Harris et al. 2011).

[2] Higher-order edge approximations have been explored in Ullrich et al. (2012).

The integration of the reconstruction function over the departure cell area is then computed. The area integration in CSLAM is transformed into a series of line integrals using the Gauss–Green theorem, and involves solving for a set of weights $w^{(i,j)}$ that depends only on the departure cell boundary. As described in Lauritzen et al. (2010), the discrete conservative transport scheme for departure cell k is

$$\int_{\delta A^*} \phi^n \, dA = \sum_{l=1}^{L_k} \left[\sum_{i+j\leq 2} c_l^{(i,j)} w_{kl}^{(i,j)} \right],$$

where $c_l^{(0,0)}$, $c_l^{(1,0)}$, $c_l^{(0,1)}$, $c_l^{(2,0)}$, and $c_l^{(0,2)}$ are the coefficients for the constant, x, z, x^2, and z^2 terms, respectively; $c_l^{(1,1)}$ is the coefficient for the xz term in Eq. (7); and l is the index for the Eulerian grid cell(s) with which departure cell k overlaps (of a total of L_k overlapping Eulerian grid cells). The partitioning of the areal integration into computation of coefficients and weights greatly enhances the transport scheme's computational efficiency for multitracer transport, as the weights can be reused for the remapping of all tracer species in the model. For full details on the basic CSLAM, see Lauritzen et al. (2010); for high-resolution spherical implementations of CSLAM, the reader is referred to the modifications to the scheme documented in Erath et al. (2013). A rigorous assessment of the accuracy of linear transport using CSLAM [for the test case in Lauritzen et al. (2012)] and a comparison of CSLAM to a collection of state-of-the-art transport schemes can be found in Lauritzen et al. (2013).

b. *Trajectory algorithm*

To find the departure cell area, we trace the vertices of each arrival grid cell back one time step Δt using a trajectory algorithm described in Lauritzen et al. (2006). The trajectory is approximated and split into two segments: departure grid point to trajectory midpoint, and trajectory midpoint to arrival grid point. The split-trajectory approximation facilitates the semi-implicit formulation of the flux-form conservation equation (section 3d).

The displacement in the two linear segments are determined using velocities at time-level n and velocities extrapolated to time-level $n + 1$, respectively. The first segment (from the departure point position $\mathbf{r}_D^n$ to midpoint trajectory $\mathbf{r}_{D/2}^{n+1/2}$) is approximated as

$$\mathbf{r}_{D/2}^{n+1/2} = \mathbf{r}_D^n + \frac{\Delta t}{2}\mathbf{v}_D^n. \tag{8}$$

We iterate Eq. (8) three times to increase the accuracy of the computation of $\mathbf{v}_D^n$. At each iteration, the velocities are interpolated to the estimated departure location using bicubic Lagrange interpolation. The second segment (from midpoint trajectory $\mathbf{r}_{D/2}^{n+1/2}$ to the arrival point $\mathbf{r}^{n+1}$) is approximated using

$$\mathbf{r}_{D/2}^{n+1/2} = \mathbf{r}^{n+1} - \frac{\Delta t}{2}\tilde{\mathbf{v}}^{n+1}, \tag{9}$$

where $\tilde{\mathbf{v}}^{n+1}$ is evaluated at the arrival grid point and denote velocities extrapolated to time-level $n + 1$ using a two-time-level extrapolation:

$$\tilde{\mathbf{v}}^{n+1} = 2\mathbf{v}^n - \mathbf{v}^{n-1}.$$

To find $\mathbf{r}_D^n$, we take the sum of the two half-trajectories [Eqs. (8) and (9)]:

$$\mathbf{r}_D^n = \mathbf{r}^{n+1} - \frac{\Delta t}{2}(\mathbf{v}_D^n + \tilde{\mathbf{v}}^{n+1}).$$

Higher-order approximations to the trajectory can be made by including an acceleration term as described in McGregor (1993). Tests including an acceleration term (not shown) showed that such a higher-order approximation made little difference to the solutions for this suite of tests.

c. *Discretization of the momentum equations*

The momentum equations are solved using the traditional semi-Lagrangian semi-implicit method, where material derivatives such as $du/dt = \partial u/\partial t + u\partial u/\partial x + w\partial u/\partial z$ and $dw/dt = \partial w/\partial t + u\partial w/\partial x + w\partial w/\partial z$ [lhs of Eqs. (1) and (2), respectively] are computed using a gridpoint interpolation to the departure point. The two-time-level discretizations of the momentum equations are

$$\begin{aligned} u_A^{n+1} = {} & \left[u - \Delta t \left(\frac{1-\beta}{2}\right) \overline{\left(\frac{\pi}{\rho_m}\right)}^x \gamma R_d \delta_x \Theta'_m \right]_D^n + \Delta t (F_u)_D^n \\ & - \Delta t \left(\frac{1+\beta}{2}\right) \overline{\left(\frac{\pi^n}{\rho_m^n}\right)}^x_A \gamma R_d \delta_x \Theta'^{n+1}_{mA}, \end{aligned} \tag{10}$$

and

$$\begin{aligned} w_A^{n+1} = {} & \left[w - \Delta t \left(\frac{1-\beta}{2}\right) \overline{\left(\frac{\pi}{\rho_m}\right)}^z \gamma R_d \delta_z \Theta'_m \right]_D^n \\ & + \frac{\Delta t}{\overline{\rho_m^n}^z} \overline{\left(g\overline{\rho}_d \frac{\pi'}{\overline{\pi}} - g\rho'_m \right)_{D/2}^{n+1/2}}^z \\ & - \Delta t \left(\frac{1+\beta}{2}\right) \overline{\left(\frac{\pi^n}{\rho_m^n}\right)}^z_A \gamma R_d \delta_z \Theta'^{n+1}_{mA} + \Delta t (F_w)_D^n, \end{aligned} \tag{11}$$

where the subscripts D, $D/2$, and A denote evaluation at the departure, midpoint trajectory, and arrival grid points, respectively, and the superscripts denote the time level. The spatial operators are defined as

$$\overline{(\cdot)}^x = \frac{1}{2}[(\cdot)_{i,k} + (\cdot)_{i+1,k}],$$

$$\overline{(\cdot)}^z = \frac{1}{2}[(\cdot)_{i,k} + (\cdot)_{i,k+1}],$$

$$\delta_x(\cdot) = \frac{(\cdot)_{i+1,k} - (\cdot)_{i,k}}{\Delta x}, \quad \text{and}$$

$$\delta_z(\cdot) = \frac{(\cdot)_{i,k+1} - (\cdot)_{i,k}}{\Delta z}.$$

The gradient terms responsible for the fast-moving acoustic waves are solved implicitly with the option of off-centering by setting $\beta \neq 0$. Numerical diffusion is represented in F_u and F_w in the form of second-order diffusion with physical viscosity ν:

$$F_{(\cdot)} = \nu[\delta_x^2(\cdot) + \delta_z^2(\cdot)].$$

The buoyancy terms in the vertical momentum equation are solved explicitly by extrapolating to time level $n + 1/2$ using

$$(\cdot)^{n+1/2} = \frac{3}{2}(\cdot)^n - \frac{1}{2}(\cdot)^{n-1},$$

and then interpolated to the midpoint trajectory. One way to evaluate the buoyancy term implicitly is to concurrently update the density and pressure perturbation variables (ρ'_m and π', respectively) at every iteration of $\tilde{\Theta}'_m$ in the Helmholtz solver. This implicit treatment of the buoyancy term involves updating the density perturbation using u^{n+1} and w^{n+1} guesses at that iteration, and we have yet to find a feasible way to incorporate this in the Helmholtz solver that ensures convergence at large time steps. The implicit treatment of the buoyancy terms will be the scope of future work.

d. Discretization of the thermodynamic equation

In our nonhydrostatic solver, we form and solve an implicit equation for Θ_m^{n+1}. The implicit equation is formed in two steps. First, we compute the explicit solution of the flux-form thermodynamic equation using the conservative transport scheme CSLAM:

$$\begin{aligned}\hat{\Theta}_m^{n+1} = \Theta_{m,\mathrm{exp}}^{n+1} &+ \frac{\Delta t}{2}\overline{[\nabla_{\mathrm{eul}} \cdot (\Theta_m^n \mathbf{v}^n) - \nabla_{\mathrm{lag}} \cdot (\Theta_m^n \mathbf{v}^n)]}\frac{\delta A^*}{\Delta A} \\ &+ \Delta t\overline{[F_{\Theta_m}^n]}\frac{\delta A^*}{\Delta A},\end{aligned} \tag{12}$$

where the notation $\overline{[\cdot]}$ denotes departure cell averages. The first term on the rhs of Eq. (12), $\Theta_{m,\mathrm{exp}}^{n+1}$, is the explicit CSLAM update. The second term is a predictor-corrector term integrated over the departure cell to account for the discrepancy between the discrete Eulerian and Lagrangian flux divergences in the semi-implicit flux-form correction term. Similarly, in F_{Θ_m}, second-order diffusion (with mixing coefficient given by ν times the Prandtl number) and the diabatic tendency from the microphysical scheme are evaluated explicitly and integrated over the departure cell area. Since the predictor-corrector and the forcing terms depend only on values at the previous time level, they can be evaluated along with $\Theta_{m,\mathrm{exp}}^{n+1}$ in a single call to CSLAM, giving $\hat{\Theta}_m^{n+1}$. Then, to allow for coupling to the momentum equations, a semi-implicit flux-form correction term is used to form the implicit equation:

$$\tilde{\Theta}_m^{n+1} = \hat{\Theta}_m^{n+1} - \frac{\Delta t}{2}[\nabla_{\mathrm{eul}} \cdot (\hat{\Theta}_m^{n+1}\mathbf{v}^{n+1}) - \nabla_{\mathrm{lag}} \cdot (\hat{\Theta}_m^{n+1}\tilde{\mathbf{v}}^{n+1})], \tag{13}$$

where $\tilde{\Theta}_m^{n+1}$ is the value of Θ_m at the new time level except for a final saturation adjustment that takes place at the end of the time step to correct the diabatic tendency using the microphysics scheme. The new tendency is then carried over to the next time step to be used as an estimate of the diabatic term in Eq. (12).

The form of the semi-implicit correction term [square-bracketed terms in Eq. (13)] stems from the split-divergence approximation used in the trajectory computation. The semi-implicit discretization for Θ_m^{n+1} is based on the flux-form scheme presented in Wong et al. (2013) for the height equation in their shallow-water equations solver. The flux-form scheme is based on the derivation of a similar semi-implicit discretization for the shallow-water model found in Lauritzen et al. (2006), but the latter scheme uses a time-independent reference state, with which it becomes difficult to ensure numerical consistency and maintain conservative properties (discussed in section 4). Instead of using a time-independent reference state, we form the semi-implicit correction term using the explicit solution $\hat{\Theta}_m^{n+1}$ from Eq. (12).

The semi-implicit correction term is defined as the difference between an Eulerian flux divergence and a Lagrangian flux divergence. On an Arakawa C-grid, these would be defined as

$$\begin{aligned}\nabla_{\mathrm{eul}} \cdot (\Theta_m \mathbf{v}) = &\frac{1}{\Delta x}[(\overline{\Theta_m}^x u)_r - (\overline{\Theta_m}^x u)_l] \\ &+ \frac{1}{\Delta z}[(\overline{\Theta_m}^z w)_t - (\overline{\Theta_m}^z w)_b],\end{aligned} \tag{14}$$

and

$$\nabla_{\mathrm{lag}} \cdot (\Theta_m \mathbf{v}) = \frac{1}{\Delta x \Delta z}\left(\overline{\Theta_m}^x \mathcal{F}_r - \overline{\Theta_m}^x \mathcal{F}_l + \overline{\Theta_m}^z \mathcal{F}_t - \overline{\Theta_m}^z \mathcal{F}_b\right), \tag{15}$$

respectively, and the $\mathcal{F}_{(\cdot)}$s are Lagrangian flux areas, where the subscripts r, l, t, and b denote the right, left, top, and bottom cell faces of an Eulerian grid cell (Fig. 2), respectively. We use an exact computation of the Lagrangian flux divergence in an Eulerian manner, where Lagrangian flux areas $\mathcal{F}_{(\cdot)}$ through each cell face are defined as

$$\mathcal{F}_r = \overline{u_r}^{zz}\Delta z - (u_{c2}w_{c3} - u_{c3}w_{c2})\Delta t/2,$$

$$\mathcal{F}_l = \overline{u_l}^{zz}\Delta z - (u_{c1}w_{c4} - u_{c4}w_{c1})\Delta t/2,$$

$$\mathcal{F}_t = \overline{w_t}^{xx}\Delta x - (u_{c3}w_{c4} - u_{c4}w_{c3})\Delta t/2,$$

$$\mathcal{F}_b = \overline{w_b}^{xx}\Delta x - (u_{c2}w_{c1} - u_{c1}w_{c2})\Delta t/2,$$

where the spatial operators are defined as

$$\overline{(\cdot)}^{xx} = \frac{1}{4}[(\cdot)_{i-1,k} + 2(\cdot)_{i,k} + (\cdot)_{i+1,k}],$$

$$\overline{(\cdot)}^{zz} = \frac{1}{4}[(\cdot)_{i,k-1} + 2(\cdot)_{i,k} + (\cdot)_{i,k+1}].$$

The terms proportional to $\Delta t/2$ correct for the geometric differences between the Eulerian and Lagrangian flux divergences (shaded areas in Fig. 2). [For full details on the derivation of $\mathcal{F}$ and $\nabla_{\mathrm{lag}} \cdot (\Theta_m \mathbf{v})$, see Wong et al. (2013).]

Using Eqs. (14) and (15), the explicit equation for $\hat{\Theta}_m^{n+1}$ in Eq. (12) and implicit equation for $\tilde{\Theta}_m^{n+1}$ in Eq. (13) can be rewritten as

$$\hat{\Theta}_m^{n+1} = \Theta_{m,\mathrm{exp}}^{n+1} + \frac{\Delta t}{2}\overline{[\nabla_{\mathrm{eul}} \cdot (\Theta_m^n \mathbf{v}'^n)]}\frac{\delta A^*}{\Delta A} + \Delta t\overline{[F_{\Theta_m}^n]}\frac{\delta A^*}{\Delta A} \tag{16}$$

and

$$\tilde{\Theta}_m^{n+1} = \hat{\Theta}_m^{n+1} - \frac{\Delta t}{2}[\nabla_{\mathrm{eul}} \cdot (\hat{\Theta}_m^{n+1}\mathbf{v}'^{n+1})], \tag{17}$$

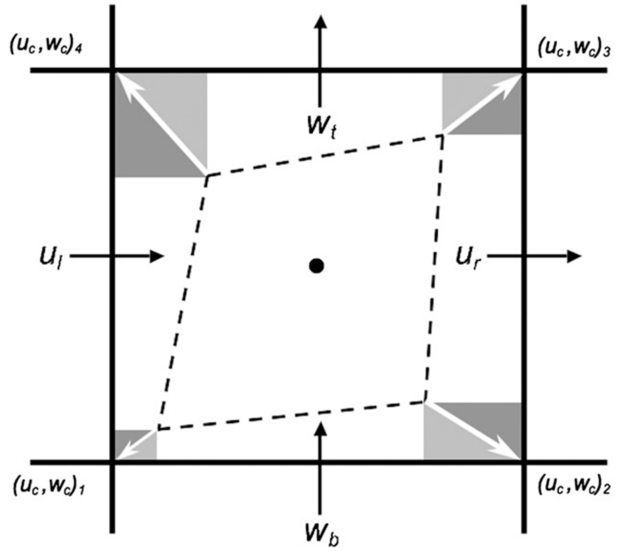

FIG. 2. Geometric representation of the Lagrangian flux divergence, defined as the flux-area difference between the Eulerian arrival grid cell (solid square) and the departure cell (dashed polygon) in one time step. Velocities associated with the Eulerian grid cell at the cell faces (u_l, u_r, w_t, w_b) and cell vertices $(u_c, w_c)_i$ for $i = 1, 2, 3, 4$ are also shown. White arrows at the four corners indicate the computed trajectories of each departure gridcell vertex.

respectively, where $\mathbf{v}'$ is a corrective velocity and

$$\nabla_{\mathrm{eul}} \cdot (\Theta_m \mathbf{v}') = \frac{1}{\Delta x}[\overline{\Theta}_m^x(u_r - \mathcal{F}_r/\Delta z) - \overline{\Theta}_m^x(u_l - \mathcal{F}_l/\Delta z)] + \frac{1}{\Delta z}[\overline{\Theta}_m^z(w_t - \mathcal{F}_t/\Delta x) - \overline{\Theta}_m^z(w_b - \mathcal{F}_b/\Delta x)].$$

e. Helmholtz equation

The Helmholtz equation with variable coefficients for the semi-implicit problem is solved using a conjugate-residual solver. Substitution of the momentum equations in Eqs. (10) and (11) into Eq. (17) forms the Helmholtz equation for $\tilde{\Theta}_m'^{n+1}$:

$$-\left(\frac{\Delta t}{2}\right)^2 \gamma R_d(1+\beta)\left[\delta_x\left(\overline{\hat{\Theta}_m^{n+1}\frac{\pi^n}{\rho_m^n}}^x \delta_x \tilde{\Theta}_m'^{n+1}\right) + \delta_z\left(\overline{\hat{\Theta}_m^{n+1}\frac{\pi^n}{\rho_m^n}}^z \delta_z \tilde{\Theta}_m'^{n+1}\right)\right] + \tilde{\Theta}_m'^{n+1} = R_\Theta - \frac{\Delta t}{2}(1+\beta)\left[\delta_x\left(\overline{\hat{\Theta}_m^{n+1}}^x R_u\right) + \delta_z\left(\overline{\hat{\Theta}_m^{n+1}}^z R_w\right)\right]. \tag{18}$$

The terms R_u, R_w, and R_Θ represent the known terms in Eqs. (10), (11), and (17), respectively. The explicit solution $\hat{\Theta}_m^{n+1}$ from CSLAM is computed prior to solving Eq. (18).

Using the explicit solution $\hat{\Theta}_m^{n+1}$ allows for a straightforward and consistent formulation between the thermodynamic and continuity equations, as long as the reconstruction of Θ_m is performed in a consistent manner. To ensure this, in CSLAM we follow Nair and Lauritzen (2010) in separating the subgridcell reconstructions for ρ_d and θ_m, and compute the second-order reconstruction function $\Theta_m(x, z)$ as

$$\Theta_m(x,z) = \langle\rho_d\rangle\theta_m(x,z) + \langle\theta_m\rangle[\rho_d(x,z) - \langle\rho_d\rangle], \qquad (19)$$

where $\langle\rho_d\rangle$ and $\langle\theta_m\rangle$ are Eulerian gridcell values, and $\rho_d(x, z)$ and $\theta_m(x, z)$ are reconstruction functions, respectively. To check for consistency, we substitute a field of constant θ_m [i.e., $\theta_m(x, z) = \langle\theta_m\rangle = 1$] in Eq. (19) and see that the rhs of Eq. (19) properly reduces to $\rho_d(x, z)$.

In summary, the solution procedure for obtaining solutions for $\tilde{\Theta}_m'^{n+1}$, u^{n+1}, and w^{n+1}, is as follows: (i) obtain solution for $\tilde{\Theta}_m'^{n+1}$ by solving the Helmholtz equation in Eq. (18); (ii) substitute solution for $\tilde{\Theta}_m'^{n+1}$ into Eqs. (10) and (11) to obtain solutions for u^{n+1} and w^{n+1}, respectively; and (iii) recalculate $\tilde{\Theta}_m'^{n+1}$ using u^{n+1} and w^{n+1} to eliminate any roundoff errors. This solution procedure is similar to that used in Wong et al. (2013) for the shallow-water equations.

f. Discretization of the continuity equation

We ensure that the flux-form thermodynamic equation is consistent with the continuity equation by using the same numerical scheme, with the inclusion of the semi-implicit correction terms in the continuity equation. Again, we first use CSLAM to obtain the explicit solution $\hat{\rho}_d^{n+1}$ in a similar manner as in Eq. (16):

$$\hat{\rho}_d^{n+1} = \rho_{d,\mathrm{exp}}^{n+1} + \frac{\Delta t}{2}\overline{[\nabla_{\mathrm{eul}}\cdot(\rho_d^n \mathbf{v}'^n)]}\frac{\delta A^*}{\Delta A}. \qquad (20)$$

Then, we add the semi-implicit correction term to Eq. (20) to be consistent with Eq. (17):

$$\rho_d^{n+1} = \hat{\rho}_d^{n+1} - \frac{\Delta t}{2}[\nabla_{\mathrm{eul}}\cdot(\hat{\rho}_d^{n+1}\mathbf{v}'^{n+1})]. \qquad (21)$$

The new time-level correction term is evaluated by back-substituting the solution of the velocity field $\mathbf{v}^{n+1}$ into $\mathbf{v}'^{n+1}$.

g. Discretization of moisture conservation equations

The flux variables of mixing ratios of water vapor q_v, cloud water q_c, and rainwater q_r are included as prognostic variables in the nonhydrostatic solver. Moist mass conservation equations are integrated using CSLAM. To ensure moisture conservation, numerical consistency between the continuity equation and the moisture conservation equations needs to be ensured. Numerical inconsistency between the continuity equation and other scalar conservation equations can lead to spurious generation or removal of scalar mass, despite using inherently mass-conserving advection schemes.

A consistent formulation of the moisture conservation equations using the scheme in Wong et al. (2013) for the flux variables $Q_j = \rho_d q_j$, where $q_j = (q_v, q_c, q_r)$ is

$$\begin{aligned}\hat{Q}_j^{n+1} = {} & Q_{j,\mathrm{exp}}^{n+1} + \frac{\Delta t}{2}\overline{[\nabla_{\mathrm{eul}}\cdot(Q_j^n \mathbf{v}'^n)]}\frac{\delta A^*}{\Delta A} \\ & + \Delta t\overline{[F_{q_j}^n]}\frac{\delta A^*}{\Delta A} \quad \text{and} \qquad (22)\end{aligned}$$

$$\tilde{Q}_j^{n+1} = \hat{Q}_j^{n+1} - \frac{\Delta t}{2}[\nabla_{\mathrm{eul}}\cdot(\hat{Q}_j^{n+1}\mathbf{v}'^{n+1})], \qquad (23)$$

where $\mathbf{v}'^n$, $\mathbf{v}'^{n+1}$, and the computations for $\nabla_{\mathrm{eul}}\cdot(\cdot)$ are the same as in Eq. (21). The explicit CSLAM solution $\hat{Q}_j^{n+1}$ [Eq. (22)] is computed using a consistent reconstruction as in Eq. (19). The quantity F_{q_j} represents second-order diffusion with a mixing coefficient same as that for Θ_m and any diabatic tendencies from the microphysics.

h. Diabatic processes

Microphysical processes are modeled using the simple warm-rain Kessler parameterization, as described in Klemp and Wilhelmson (1978). In the evaluation of the thermodynamic and moisture conservation equations, the diabatic forcing is approximated in F_{Θ_m} and F_{Q_j} [Eqs. (16) and (22), respectively] using the most up-to-date values integrated over the departure cell. These values are then removed from the solutions prior to calling the Kessler microphysics scheme. The included microphysical processes are 1) condensation of water vapor into cloud water, 2) autoconversion by diffusion and collection of cloud water into rainwater, 3) evaporation of cloud water and rain, and 4) precipitation of rain, which is removed when it reaches the surface. These microphysical processes are computed as a final adjustment at the end of the time step, advancing $\tilde{\Theta}_m^{n+1}$ and $\tilde{Q}_j^{n+1}$ to Θ_m^{n+1} and Q_j^{n+1} in a manner that is consistent with saturation conditions at the new time level.

i. Diagnostic equation of state

Pressure is a diagnostic variable computed using the equation of state in Eq. (6):

$$p = p_0\left(\frac{R_d\Theta_m}{p_0}\right)^{\gamma},$$

where p_0 is the reference surface pressure set to 100 kPa.

j. Consistency and shape preservation

In the CSLAM reconstruction step, we reconstruct Q_j using Eq. (19) described in section 3e to ensure consistency. To ensure shape preservation, we follow the two steps as described in Wong et al. (2013). First, we use the simple 2D filter by Barth and Jespersen (1989) that searches for new local minima and maxima in the reconstruction function of a scalar field such as moisture mixing ratio q_j, and scales the function if these values exceed those in the neighboring cell. For chemistry applications, preservation of linear correlations in tracers is important, and it has been found that the limiter preserves linear correlations between tracers, whereas typically linear correlation is only preserved when the limiter is not applied. Second, to ensure shape preservation in the flux-divergence terms, we compute the upwind moist species mixing ratio q_j^* by first decoupling Q_j from ρ_d. Then, the flux divergences are computed by centering density to each of the cell faces:

$$\nabla_{\text{eul}} \cdot \rho_d q_j \mathbf{v}' = \frac{1}{\Delta x}[(\overline{\rho}_d^x q_j^* u')_r - (\overline{\rho}_d^x q_j^* u')_l] + \frac{1}{\Delta z}[(\overline{\rho}_d^z q_j^* w')_t - (\overline{\rho}_d^z q_j^* w')_b].$$

The upwind q_j^* values are determined using $\mathbf{v}'$.

4. Desirable properties of CSLAM-NH

The flux-form nonhydrostatic semi-implicit CISL solver CSLAM-NH has six main advantages and desirable properties: (i) is inherently mass conserving using the conservative semi-Lagrangian transport scheme CSLAM, (ii) ensures numerically consistent transport, (iii) is independent of a mean reference state, (iv) is shape preserving, and (v) like typical semi-implicit solvers, CSLAM-NH requires solving a single linear Helmholtz equation and (vi) a single application of CSLAM at each time step.

CSLAM-NH uses a formulation of the discretized continuity equation that ensures numerical consistency for a CISL solver. In CSLAM-NH, a Helmholtz equation for the potential temperature perturbation is solved. Traditionally, to avoid solving a nonlinear Helmholtz equation, the flux divergence term that is coupled to the momentum equations is often first linearized around a mean reference state $\Theta_{m,\text{ref}}$:

$$\Theta_m^{n+1} = \Theta_{m,\exp}^{n+1} - \frac{\Delta t}{2}[\nabla_{\text{eul}} \cdot (\Theta_{m,\text{ref}} \mathbf{v}'^{n+1})] + \frac{\Delta t}{2}\overline{[\nabla_{\text{eul}} \cdot (\Theta_{m,\text{ref}} \mathbf{v}'^{n})]}\frac{\delta A^*}{\Delta A} + \Delta t \overline{[F_{\Theta_m}^n]}\frac{\delta A^*}{\Delta A}, \tag{24}$$

where $\Theta_{m,\text{ref}}$ is a mean reference state that is often time independent and varies with height. A choice of reference state can be the hydrostatic background state $\overline{\rho}_d\overline{\theta}$. The scheme in Eq. (24) is a nonhydrostatic extension to the SWE semi-implicit CISL continuity equation in Lauritzen et al. (2006).

To ensure conservation of potential temperature, it is important for the discrete thermodynamic equation to be numerically consistent with the discrete continuity equation. A discretized continuity equation numerically consistent with Eq. (24) is

$$\rho_d^{n+1} = \rho_{d,\exp}^{n+1} - \frac{\Delta t}{2}[\nabla_{\text{eul}} \cdot (\rho_{d,\text{ref}} \mathbf{v}'^{n+1})] + \frac{\Delta t}{2}\overline{[\nabla_{\text{eul}} \cdot (\rho_{d,\text{ref}} \mathbf{v}'^{n})]}\frac{\delta A^*}{\Delta A}. \tag{25}$$

Transported material, such as moisture and passive tracers with some mixing ratio q, are often solved explicitly using the CISL transport scheme:

$$\phi^{n+1} = \phi_{\exp}^{n+1} + \Delta t \overline{[F_\phi^n]}\frac{\delta A^*}{\Delta A}, \tag{26}$$

where $\phi = \rho_d q$ is the scalar mass and $\overline{[F_\phi^n]}$ represents diffusion and any diabatic tendency evaluated at time level n over the departure cell. Such explicit schemes would lead to numerical inconsistency between the discrete CISL continuity equation in Eq. (25) and the discrete constituent mass conservation equations such as in Eq. (26). If the discrete conservation equation is consistent with the discrete continuity equation, the former should reduce to the latter when q is a constant, and an initially spatially uniform passive tracer field should remain so. The inconsistent flux-divergence correction term in Eq. (25) can spuriously generate or remove moisture or tracer mass in the model.

Alternatively, one can formulate the discrete scalar conservation equation in a manner consistent with Eq. (25) by including the flux-divergence correction terms:

$$\phi^{n+1} = \phi_{\exp}^{n+1} - \frac{\Delta t}{2}[\nabla_{\text{eul}} \cdot (\phi_{\text{ref}} \mathbf{v}'^{n+1})] + \frac{\Delta t}{2}\overline{[\nabla_{\text{eul}} \cdot (\phi_{\text{ref}} \mathbf{v}'^{n})]}\frac{\delta A^*}{\Delta A} + \Delta t \overline{[F_\phi^n]}\frac{\delta A^*}{\Delta A}. \tag{27}$$

However, determining an appropriate choice for reference state ϕ_{ref} is difficult, making a numerically consistent formulation such as in Eq. (27) hard to implement.

The formulations we present for the thermodynamic, density, and moisture conservation equations [Eqs. (17), (21), and (23), respectively] are all numerically consistent with one another. These consistent formulations are made possible by avoiding the use of a mean reference state. In our formulation, we use the explicit CSLAM solution instead of a mean reference state in the flux-divergence correction terms. This approach eliminates the difficult choice of a mean reference state ϕ_{ref} for moisture or tracer mass.

Even if an appropriate choice of ϕ_{ref} can be found, using a time-independent mean reference state in Eq. (27) can be problematic for regions with little moisture or tracer mass ($\hat{\phi}^{n+1} \ll 1$). Depending on the magnitude of ϕ_{ref}, the flux divergences are likely nonzero for a divergent flow and can, therefore, generate or remove unphysical mass (Lauritzen et al. 2008). In the nonhydrostatic solver presented here, by computing the flux divergences of the explicit solution $\hat{\phi}^{n+1}$, the magnitude of the flux divergences are better approximated for regions with little moisture or tracer mass.

As scalar mass conservation is not guaranteed in an inconsistent solver, these solvers also generally do not preserve the shape of scalar fields such as mixing ratios, even when shape-preserving filters are applied to the transport scheme. The implications are that the scalar field may no longer be positive-definite, and new unphysical minima and maxima can occur because of under- and overshooting, respectively. The consistent and shape-preserving transport in the proposed solver ensures that no new (unphysical) minimum and maximum (within machine roundoff) will occur.

5. Idealized test cases

Two of the three idealized test cases presented—namely, a density current simulation and a gravity wave simulation—are commonly used as benchmarks for testing nonhydrostatic solvers. The third idealized test case is a 2D squall-line simulation, where the stability of the model is tested with latent heating modeled by a simple warm-rain microphysics scheme. In addition to comparing with available solutions in the literature, comparisons with an Eulerian split-explicit model with second-order advection are also presented.

a. Density current

The nonlinear density current test case, described in Straka et al. (1992), is widely used as a benchmark test for nonhydrostatic solvers (e.g., Klemp et al. 2007; Xue et al. 2000). An initial cold temperature perturbation is centered in the domain, and the negatively buoyant cold air descends to the surface and forms symmetric density currents propagating in opposite directions. Straka et al. (1992) provides a well-documented comparison among various compressible and quasi-compressible solvers as well as a high-resolution benchmark solution.

The numerical domain is centered at $x = 0.0\,\mathrm{km}$, with $-25.6 \le x \le 25.6\,\mathrm{km}$ and $0 \le z \le 6.4\,\mathrm{km}$. As described in Straka et al. (1992), the initial condition is given by a temperature perturbation ΔT:

$$\Delta T = \begin{cases} 0.0^\circ\mathrm{C}, & \text{if} \quad L \ge 1.0 \\ -15.0^\circ\mathrm{C}[\cos(\pi L) + 1.0]/2, & \text{if} \quad L < 1.0 \end{cases} \quad \text{and}$$

$$L = \sqrt{[(x - x_c)/x_r]^2 + [(z - z_c)/z_r]^2},$$

where $(x_c, z_c) = (0.0, 3.0)$ km is the center of the perturbation, and its width and depth are given by $x_r = 4.0\,\mathrm{km}$ and $z_r = 2.0\,\mathrm{km}$. The surface temperature θ_0 is at 300 K in a horizontally homogeneous and neutral environment. A constant physical viscosity of $75\,\mathrm{m}^2\,\mathrm{s}^{-1}$ is used. The domain is an x-periodic channel with reflective boundary conditions along the upper and lower boundaries as specified by Straka et al. (1992) that require $\partial u/\partial z = w = \partial \rho/\partial z = \partial \Theta/\partial z = 0$.

Following Straka et al. (1992), we simulate the density current test case using grid spacings $\Delta x = \Delta z = 400, 200, 100, 50,$ and 25 m, with Eulerian time step sizes of $\Delta t = 4, 2, 1, 0.5,$ and 0.25 s, respectively. Figure 3 shows the potential temperature perturbation (θ') from its mean state from CSLAM-NH and the Eulerian split-explicit scheme with second-order advection at the simulation end time of 15 min using different model resolutions.

The density current is clearly underresolved using a 400-m grid spacing, with only the main rotor marginally resolved ($7 \le x \le 9\,\mathrm{km}$). A grid spacing of 200 m gives a better resolution of the main rotor as well as a second rotor ($11 \le x \le 12\,\mathrm{km}$); however, the leading third rotor is still underresolved. For resolutions finer than $\Delta x = \Delta z = 100\,\mathrm{m}$, all three rotors are well resolved with the solutions converging and indistinguishable by eye between 50- and 25-m grid spacings. The differences among the model resolutions agree well with those documented in other nonhydrostatic solvers such as in Straka et al. (1992), Xue et al. (2000), Skamarock and Klemp (2008), and Melvin et al. (2010).

Positions of the density current front (specified to be at $\theta' = -1\,\mathrm{K}$), the minimum and maximum θ' values in the domain, and $\boldsymbol{\Sigma}\theta'_{\mathrm{sampled}}$ for all $\theta'_{\mathrm{sampled}}$ and $\theta'_{\mathrm{sampled}} > 0$, and $\boldsymbol{\Sigma}\theta'^{2}_{\mathrm{sampled}}$ are shown in Table 1. We also compare the results with those from the nonhydrostatic vertical-slice solver that uses the Semi-Lagrangian Inherently Conserving and Efficient (SLICE) scheme (Table II of Melvin et al. 2010) and the 25-m fully compressible Eulerian reference (REFC25) model in Straka et al. (1992) (Table IV of Straka et al. 1992). In computing the summation statistics, $\theta'_{\mathrm{sampled}}$ from each of the

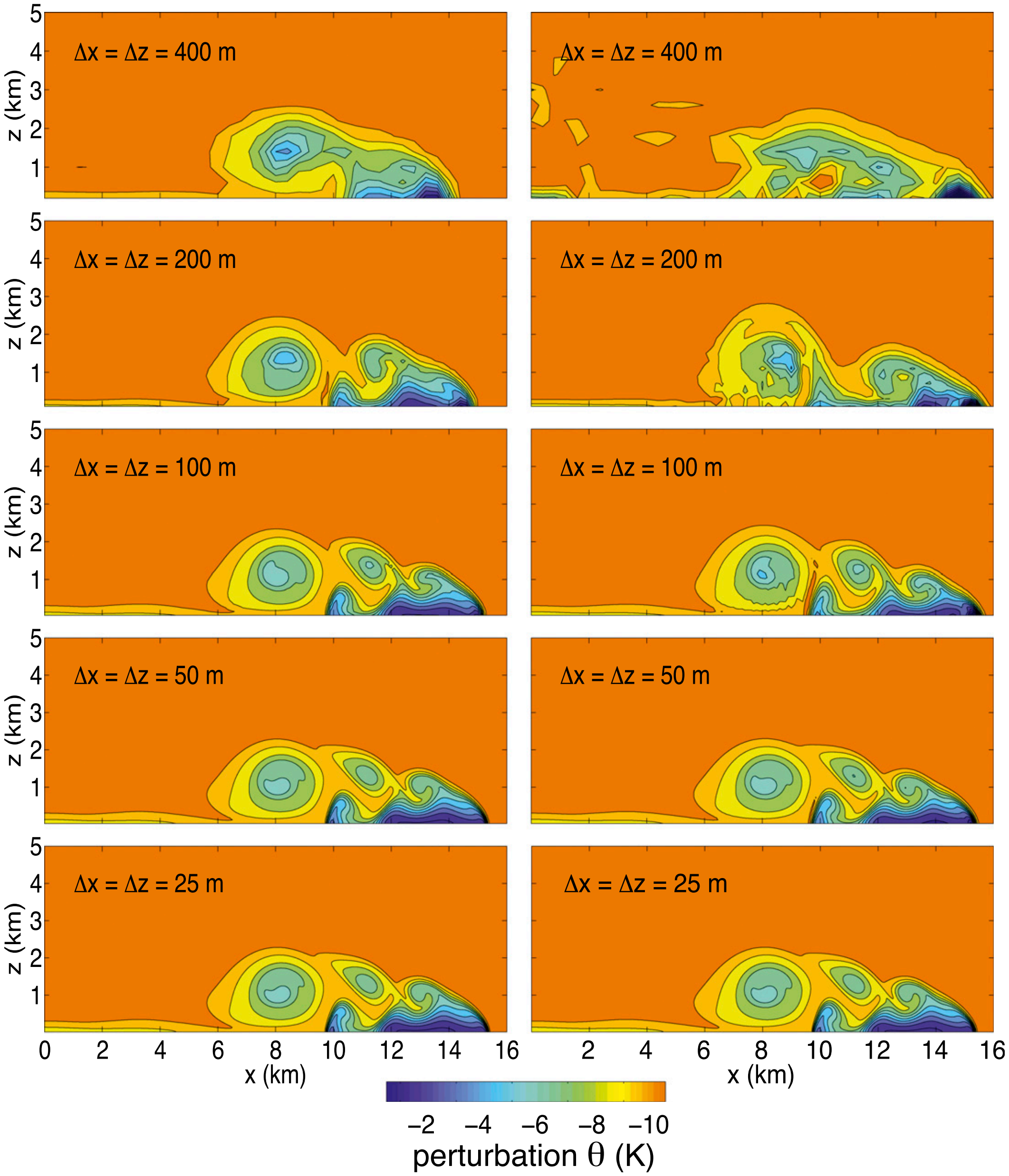

FIG. 3. Potential temperature perturbation (K) after 15 min for (left) CSLAM-NH and (right) the Eulerian split-explicit scheme for (from top to bottom) $\Delta x = \Delta z = 400, 200, 100, 50$, and 25 m. Contour intervals are every 1 K, starting at 0.5 K. Mean wind $\overline{U} = 0\,\mathrm{m\,s^{-1}}$.

CSLAM-NH runs (except for the 400-m grid-spacing run) are sampled at 200-m resolution. This sampling is done so that we can make a direct comparison with the statistics of REFC25 in Straka et al. (1992) (where they sampled REFC25 at 200-m resolution). Statistics from the 25-m solution agree closely with the nonhydrostatic SLICE model, with a similar slight discrepancy in the density front location when compared to REFC25. Both CSLAM-NH and SLICE are semi-Lagrangian models with inherent dissipation and order of accuracy different from REFC25, an Eulerian compressible solver with second-order advection; these differences could lead to the slight discrepancy in the density front locations. In addition to model differences, like the SLICE model, a different time step size is used to compute the 25-m solution (16 times larger than that used to compute REFC25). At coarser resolutions (400 and 200 m), the minimum θ' values are colder than those in SLICE; therefore, the front locations also traveled farther out from the center line. Analytically, the maximum θ' should

TABLE 1. Statistics for the density current simulations at time 15 min using CSLAM-NH at various grid resolutions and time steps. Comparison values from the nonhydrostatic x–z solver using SLICE in Melvin et al. (2010) are also presented. REFC25 are values taken from Straka et al. (1992). The θ'_{sampled} are solutions sampled at 200 m for comparison with values in Straka et al. (1992).

$\Delta x = \Delta z$ (m)	Δt (s)	$\theta'_{\min}$ (K)	$\theta'_{\max}$ (K)	Front location (m)	$\Sigma\theta'_{\text{sampled}}$ (K)	$\Sigma\theta'_{\text{sampled}}$ (for $\theta' > 0$) (K)	$\Sigma\theta'^{2}_{\text{sampled}}$ (K^2)
400	4	−10.339	0.6804	14 248	—	—	—
200	2	−10.746	0.0846	14 938	−1293.82	4.4398×10^{-1}	5634.92
100	1	−9.7694	0.0006	15 234	−1361.41	1.8114×10^{-4}	6127.90
100	4	−9.6985	0.0053	15 256	−1360.73	6.7741×10^{-3}	6182.03
50	0.5	−9.7078	0.0000	15 360	−1394.93	2.0562×10^{-5}	6395.63
25	0.25	−9.7323	0.0000	15 391	−1411.62	3.2974×10^{-8}	6516.33
SLICE400	4	−5.6608	0.3674	13 572	—	—	—
SLICE200	2	−8.0958	0.1226	14 768	—	—	—
SLICE100	1	−9.8574	0.0995	15 182	—	—	—
SLICE50	0.5	−9.4995	0.0626	15 334	—	—	—
SLICE25	0.25	−9.6548	0.0048	15 390	—	—	—
REFC25	0.015 625	−9.7738	0.0000	15 537	−1427.10	0.0000	6613.62

remain zero throughout the simulation, as is the case in the higher-resolution runs (50 and 25 m). The contribution of positive θ' values in $\boldsymbol{\Sigma}\theta'_{\text{sampled}}$ is also small at these resolutions (in the order of 1×10^{-5} K and 1×10^{-8} K, respectively), increasing up to the order of 1×10^{-1} K at 200 m. [Straka et al. (1992) only reported values up to four decimal points.]

For the next simulation, a mean background wind of $\overline{U} = 20\,\text{m}\,\text{s}^{-1}$ is applied to the described test case, as is done in Skamarock and Klemp (2008) to examine phase errors. Solutions from CSLAM-NH and the Eulerian split-explicit second-order advection scheme of both the left- and right-moving currents at time 15 min using $\Delta x = \Delta z = 200$, 100, and 50 m are shown in Fig. 4. Time step sizes are the same as in Fig. 3. The solutions from CSLAM-NH in general show proper symmetry about the translating centerline, although very subtle differences between the secondary rotors in the left- and right-moving currents are noticeable at 200- and 100-m grid spacing. As a comparison, the Eulerian split-explicit second-order advection scheme shows noticeably larger errors in the right-moving current as expected because of the right-moving current moving at a greater speed than the other (causing larger advective phase errors).

For this test case, we found that the maximum stable time step size in CSLAM-NH is double of that of the Eulerian scheme. Figure 5 shows solutions for tests where $\overline{U} = 0\,\text{m}\,\text{s}^{-1}$ at $\Delta x = \Delta z = 100$ m using a time step size of 3 and 4 s, whereas the maximum stable Eulerian time step size is $\Delta t = 2$ s. The solution using a large time step of 4 s is almost indistinguishable by eye from the 25-m high-resolution solutions (Fig. 3). With mean advection ($\overline{U} = 20\,\text{m}\,\text{s}^{-1}$), the maximum stable time step in CSLAM-NH is 3 s. As we increase the time step size to 4 s, the phase error was large enough to form unphysically steep gradients at the leading edge of the right-moving current, which then caused the violation of the Lipschitz stability condition. The maximum stable time

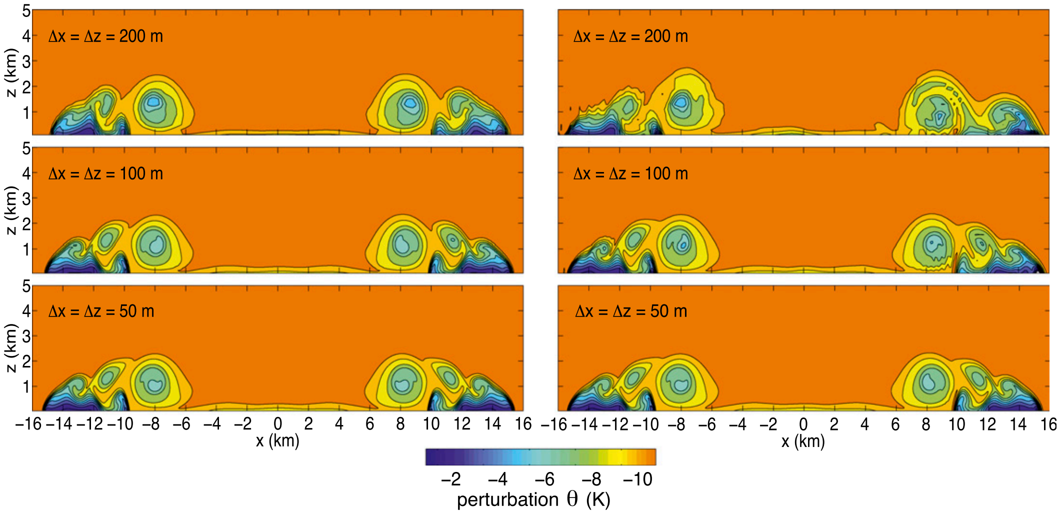

FIG. 4. As in Fig. 3, but for (from top to bottom) $\Delta x = \Delta z = 200$, 100, and 50 m and a mean wind $\overline{U} = 20\,\text{m}\,\text{s}^{-1}$.

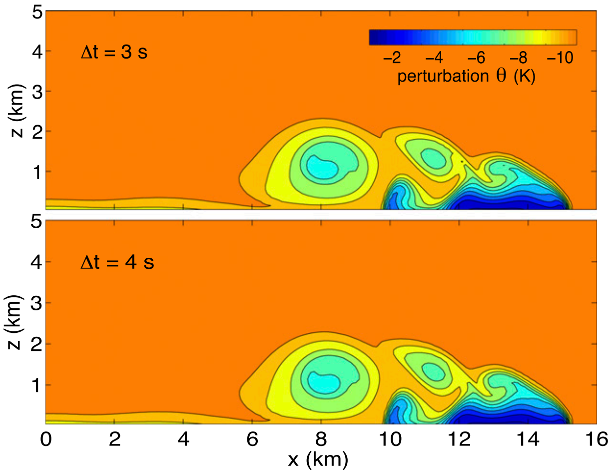

FIG. 5. Potential temperature perturbation (K) from CSLAM-NH after 15 min for grid spacing $\Delta x = \Delta z = 100$ m using time step sizes $\Delta t =$ (top) 3 and (bottom) 4 s. Mean wind $\overline{U} = 0\,\mathrm{m\,s^{-1}}$. The Eulerian split-explicit scheme (not plotted) was numerically unstable for these time steps, as it required $\Delta t \le 2$ s for numerical stability of this gravity current. Contoured as in Fig. 3.

step in the Eulerian model is 1.5 s. Using a time step size of 5 s, instability was observed in the vicinity of the leading edge of the subsiding cold air for both cases with and without the mean wind.

b. *Gravity wave*

A second test case of a gravity wave in a periodic channel with solid, free-slip upper- and lower-boundary conditions is used to evaluate the nonhydrostatic solver. The test case is described in Skamarock and Klemp (1994), where they presented results for a Boussinesq atmosphere. The test case is characterized by an initial potential temperature perturbation of amplitude $\Delta\theta_0$:

$$\theta(x, z, t = 0) = \Delta\theta_0 \frac{\sin(\pi z/H)}{1 + (x - x_c)^2/a^2},$$

where $\Delta\theta_0 = 10^{-2}$ K, $a = 5$ km is the half-width of the initial perturbation, $H = 10$ km is the total depth of the domain, and $x_c = 0.25L$, where $L = 300$ km is the length of the domain. The background atmospheric stratification has a constant Brunt–Väisäla frequency $N = 10^{-2}\,\mathrm{s^{-1}}$. For one simulation, no mean wind ($\overline{U} = 0$) is prescribed. The other simulation uses a mean wind of $\overline{U} = 20\,\mathrm{m\,s^{-1}}$, advecting the solution to the right while the two gravity wave modes propagate in opposite directions. Again, the mean advection of the solution accentuates any advective phase speed errors in the scheme. The boundary condition is implemented by linear extrapolating u, Θ, and ρ values into the boundary, consistent with the free-slip boundary conditions, and setting $w = 0$.

We run the gravity wave test case at grid spacings $\Delta x = \Delta z = 1$ km, 500 m, and 250 m using Eulerian time step sizes $\Delta t = 12$, 6, and 3 s, respectively. Solutions from CSLAM-NH at the three resolutions for $\overline{U} = 0$ (not shown) are indistinguishable by eye from the 250- and 500-m solutions for $\overline{U} = 20\,\mathrm{m\,s^{-1}}$ in Fig. 6 and compare well with those using the Advanced Research Weather Research and Forecasting Model (ARW-WRF; solutions using the fifth- and sixth-order advection scheme are available online at http://www.mmm.ucar.edu/projects/srnwp_tests/IG_waves/ig_wave.html), with the second-order advection scheme of the same Eulerian split-explicit scheme (not shown), and with the SLICE nonhydrostatic vertical model in Melvin et al. (2010). In Skamarock and Klemp (1994), the solution presented for this nonhydrostatic test case uses a Boussinesq model, where the symmetry of the analytic Boussinesq solution in both x and z is maintained. The density variation in the full Euler equations results in solutions that are asymmetric in z, as observed in the CSLAM-NH solutions, the second-order Eulerian solutions, the fifth-order Eulerian solutions, as well as the SLICE nonhydrostatic vertical model solutions.

Like in the density current test, we impose a mean advection wind $\overline{U} = 20\,\mathrm{m\,s^{-1}}$ to examine phase errors. These tests are made at the same grid spacings and time step sizes as in the no mean wind case. The right- and left-moving waves from CSLAM-NH exhibit nearly perfect symmetry, indicating there is minimal phase error in the solutions. The Eulerian split-explicit second-order advection scheme shows more noticeable phase errors (Fig. 6).

Testing of CSLAM-NH using larger time steps in this gravity wave test case reveals a numerical stability condition that is sensitive to the stratification N. (We note that CSLAM-NH is unconditionally stable for $N = 0$, i.e., for a near-pure advection case of the initial warm perturbation.) Figure 7 shows the instability for $N = 0.01\,\mathrm{s^{-1}}$ with and without a mean wind imposed. We further evaluate the maximum stable CSLAM-NH time step size for the gravity wave case with the mean advection wind speed of $\overline{U} = 20\,\mathrm{m\,s^{-1}}$ ($\Delta x = \Delta z = 1$ km) over a range of N (0.01, 0.015, and 0.02 $\mathrm{s^{-1}}$). Since the gravity wave phase speed varies with N, we increase/decrease the simulation time length as appropriate such that the gravity wave solutions are similar to those shown in Fig. 6; for example, for $N = 0.015\,\mathrm{s^{-1}}$, the simulation time is reduced to 2000 s. Test results showed that the maximum stable CSLAM-NH time step sizes are $\Delta t_{\max} = 38$, 35, and 32 s for $N = 0.01$, 0.015, and 0.02 $\mathrm{s^{-1}}$, respectively, whereas in the case of the Eulerian split-explicit scheme, the maximum stable large time steps are found to be $\Delta t = 60$, 55, and 50 s (with small time step size of 2.4 s), respectively,

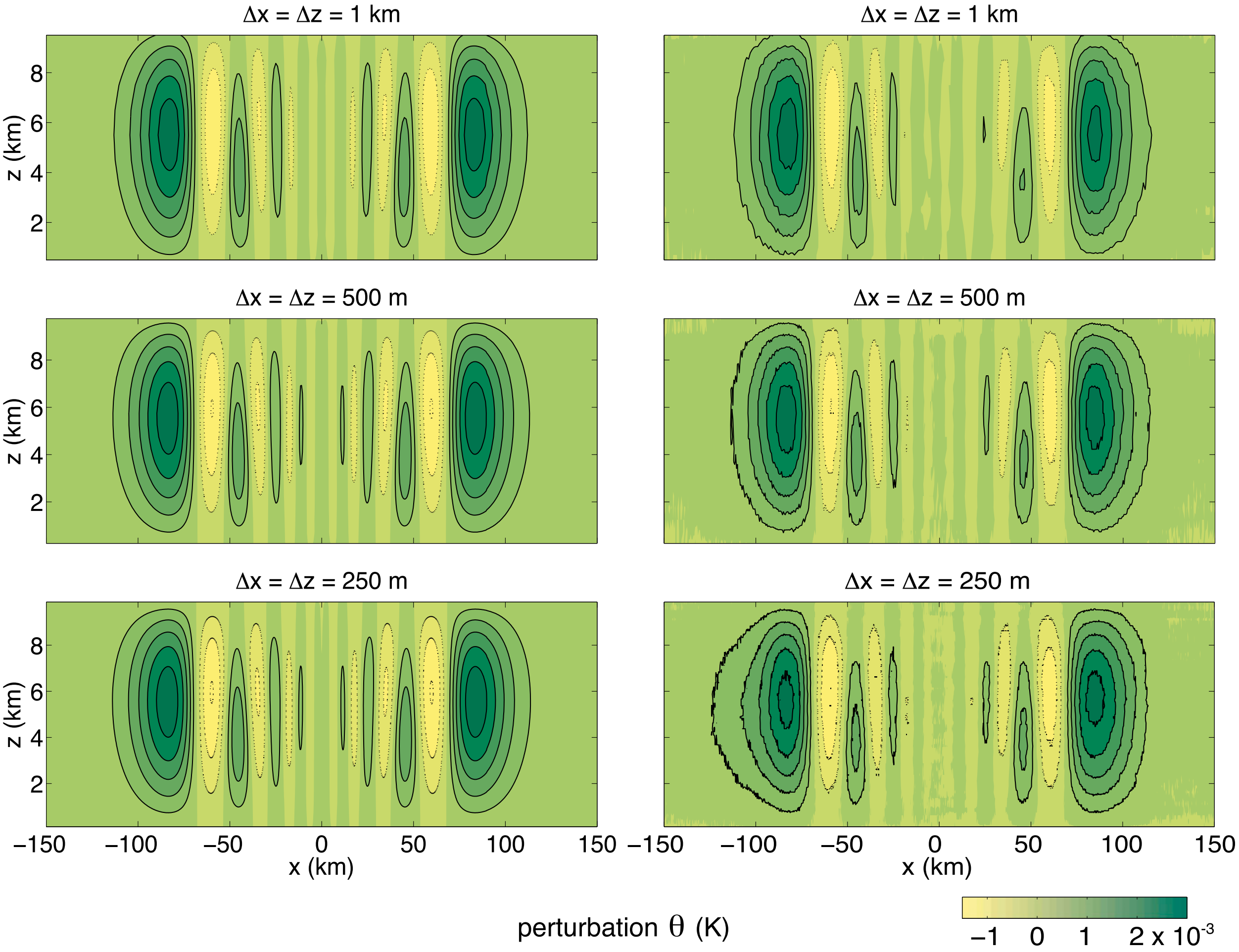

FIG. 6. Potential temperature perturbation (K) after 50 min for (left) CSLAM-NH and (right) the Eulerian split-explicit scheme for (from top to bottom) $\Delta x = \Delta z = 1000$, 500, and 250 m. Contour interval is 5×10^{-4} K (zero contour line not plotted). Solid lines indicate positive contours and dashed lines indicate negative contours. Solution is translated using a mean wind $\overline{U} = 20\,\mathrm{m\,s^{-1}}$. Horizontal axis has also been translated with the mean wind so the line of symmetry remains at $x = 0$.

limited by the stability condition of the advection scheme. The buoyancy terms in the vertical momentum equation are integrated explicitly in CSLAM-NH, and handled implicitly in the Eulerian scheme. When we remove the buoyancy terms from the implicit step and solve them explicitly in the Eulerian model, the time step sizes required to obtain solutions of similar accuracy as those from the vertically implicit model are reduced by 20%–35%, and are closer to those found in CSLAM-NH. The devising of an integration scheme that handles the buoyancy terms implicitly in CSLAM-NH will require a robust and stable way of updating the density perturbation in the Helmholtz solver, and this will be addressed in future work.

c. 2D (x–z) squall line

We perform a test case of a 2D squall line as described in Weisman and Klemp (1982) to evaluate mass conservation, consistency, and shape-preservation in the nonhydrostatic solver, in addition to testing for any small-scale computational instability in the model due to latent heating.

The numerical domain is centered at $x = 0.0$ km, with $-100 \le x \le 100$ km and $0 \le z \le 20$ km. As in Weisman and Klemp (1982), a conditionally unstable thermodynamic profile is used to initialize the horizontally homogeneous environment. Constant physical horizontal and vertical eddy viscosities of $250\,\mathrm{m^2\,s^{-1}}$ are used. A warm thermal perturbation near the surface is prescribed to initiate convection (Weisman et al. 1988). The initial thermal perturbation has a maximum of $\Delta\theta_0 = 3$ K, centered at $z_c = 1.5$ km and along the center line ($x_c = 0$) of the domain, with a horizontal radius x_r of 10 km and a vertical radius z_r of 1.5 km. The shape of the perturbation is a cosine hill given as

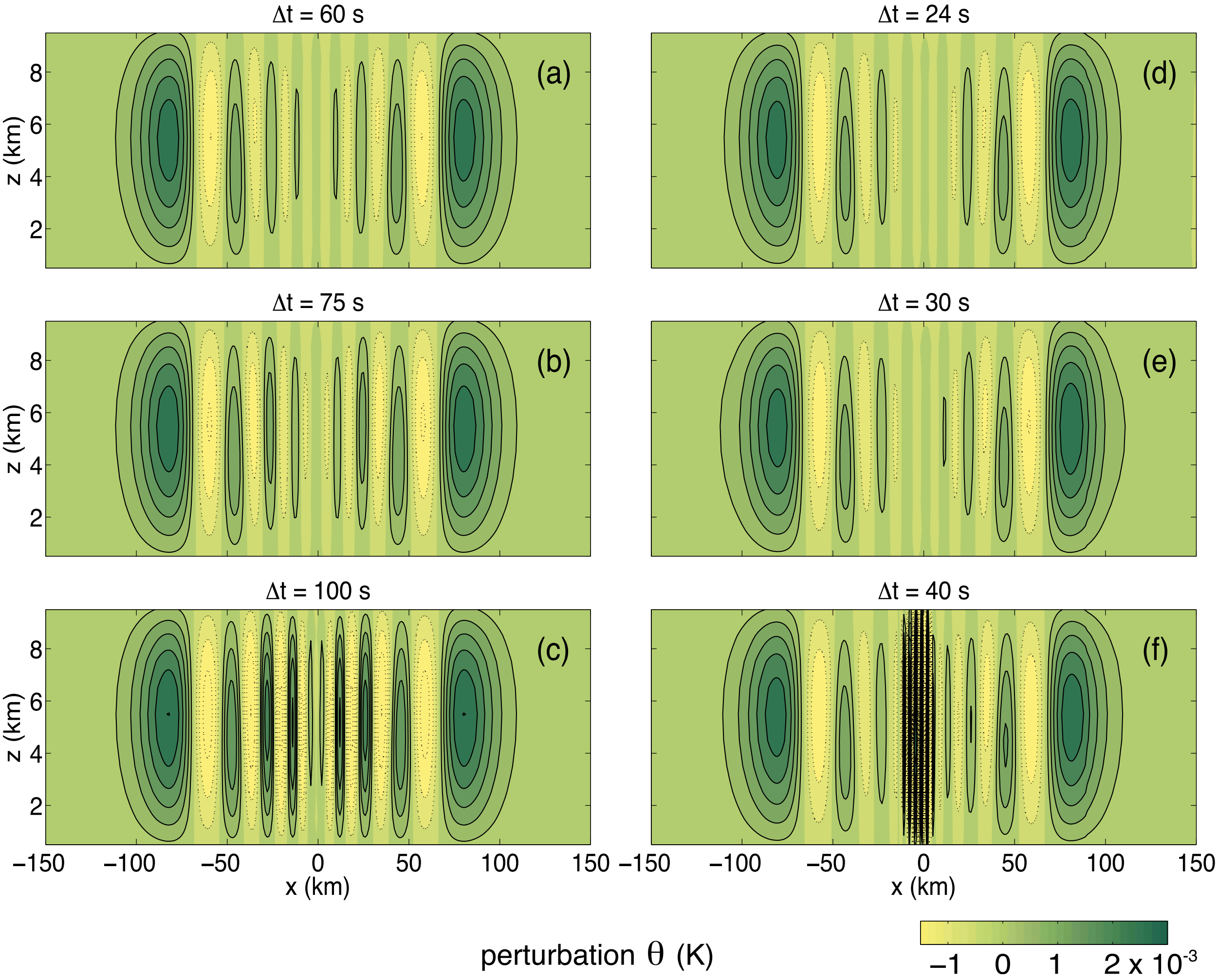

FIG. 7. Potential temperature perturbation (K) solutions of the gravity wave case using increasingly large CSLAM-NH time steps ($\Delta x = \Delta z = 1$ km) where (a)–(c) $\overline{U} = 0\,\mathrm{m\,s^{-1}}$ with (from top to bottom) $\Delta t = 60$–100 s and (d)–(f) $\overline{U} = 20\,\mathrm{m\,s^{-1}}$ with (from top to bottom) $\Delta t = 24$–40 s. Contoured as in Fig. 6.

$$\theta(x, z, t=0) = \begin{cases} \Delta\theta_0 \cos^2(\pi L/2), & L < 1.0 \\ 0, & L \geq 1.0 \end{cases} \quad \text{and}$$

$$L = \sqrt{(x/x_r)^2 + [(z - z_c)/z_r]^2}.$$

A weak vertical wind shear within a 2.5-km layer at the surface is used to promote the growth of the squall line. The initial wind profile is given as

$$u(z, t=0) = \begin{cases} \overline{u} \cdot (z/z_{\mathrm{ts}}) - u_s, & z < z_{\mathrm{ts}} \\ \overline{u} - u_s, & z \geq z_{\mathrm{ts}}, \end{cases}$$

where $\overline{u} = 12\,\mathrm{m\,s^{-1}}$, $u_s = 10\,\mathrm{m\,s^{-1}}$, and $z_{\mathrm{ts}} = 2.5$ km. The environmental potential temperature and relative humidity profiles at the initial time are

$$\overline{\theta}(z, t=0) = \begin{cases} \theta_0 + (\theta_{\mathrm{tr}} - \theta_0)(z/z_{\mathrm{tr}})^{5/4}, & z \leq z_{\mathrm{tr}} \\ \theta_{\mathrm{tr}} \exp\left[\dfrac{g}{c_p T_{\mathrm{tr}}}(z - z_{\mathrm{tr}})\right], & z > z_{\mathrm{tr}} \end{cases}$$

and

$$\mathrm{RH}(z, t=0) = \begin{cases} 1 - \dfrac{3}{4}(z/z_{\mathrm{tr}})^{5/4}, & z \leq z_{\mathrm{tr}} \\ 0.25, & z > z_{\mathrm{tr}}, \end{cases}$$

where $\theta_{\mathrm{tr}} = 343$ K, $z_{\mathrm{tr}} = 12.0$ km, and $T_{\mathrm{tr}} = 213$ K are the potential temperature, geometric height, and actual temperature at the tropopause, respectively. The maximum water mixing ratio is capped at $14\,\mathrm{g\,kg^{-1}}$. The surface potential temperature $\theta_0 = 300$ K. The skew

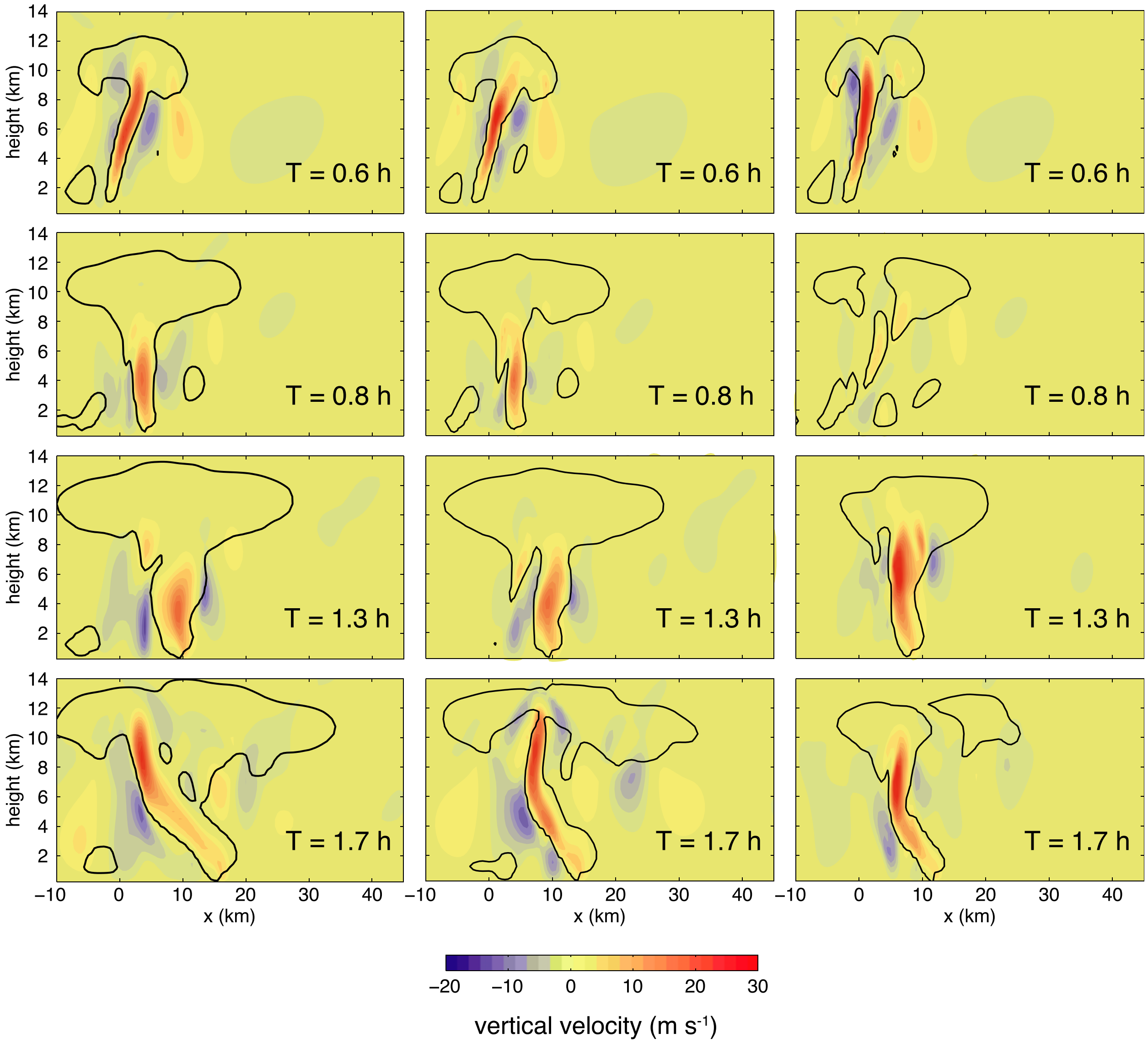

FIG. 8. Vertical cross sections of vertical velocity (color shading; m s^{-1}) and solid contours of the convective cloud structure (q_c = 0.1 g kg^{-1}) at times (from top to bottom) T = 0.6, 0.8, 1.3, and 1.7 h of the simulation for the 500-m grid-spacing runs with a Δt = 5.0 s from (left) CSLAM-NH, (middle) fifth-order split-explicit Eulerian model, and (right) second-order split-explicit Eulerian model.

T–log$p$ diagram for this sounding can be found in Fig. 1 of Weisman and Klemp (1982). Numerical simulations (unless otherwise stated) use a grid spacing $\Delta x = \Delta z$ = 500 m, a time step Δt = 5 s, and a time-off-centering parameter of $\beta = 0.1$ to maintain numerical stability. Like the gravity case, the boundary condition is implemented by linear extrapolating u, Θ, and ρ values into the boundary and setting $w = 0$, consistent with the free-slip boundary conditions.

A comparison of the squall-line development among CSLAM-NH (with shape preservation), the fifth-order split-explicit, and the second-order split-explicit Eulerian models is presented in Fig. 8. Instantaneous and accumulated surface precipitation integrated across the model domain are presented in Fig. 9; also shown is the rate of condensation over the entire domain. Maximum updraft velocity is shown in Fig. 10. The series of updraft velocity peaks highlight the continuous triggering of new convective systems along the advancing front.

All three models (CSLAM-NH, Eulerian fifth-order advection, and Eulerian second-order advection) show similar development of the convective system (Fig. 8). At 0.6 h, all three models show an initial downshear orientation of the system due to the ambient wind shear. As the storm continues to develop with the cold pool strengthening behind the system (not shown), convergence

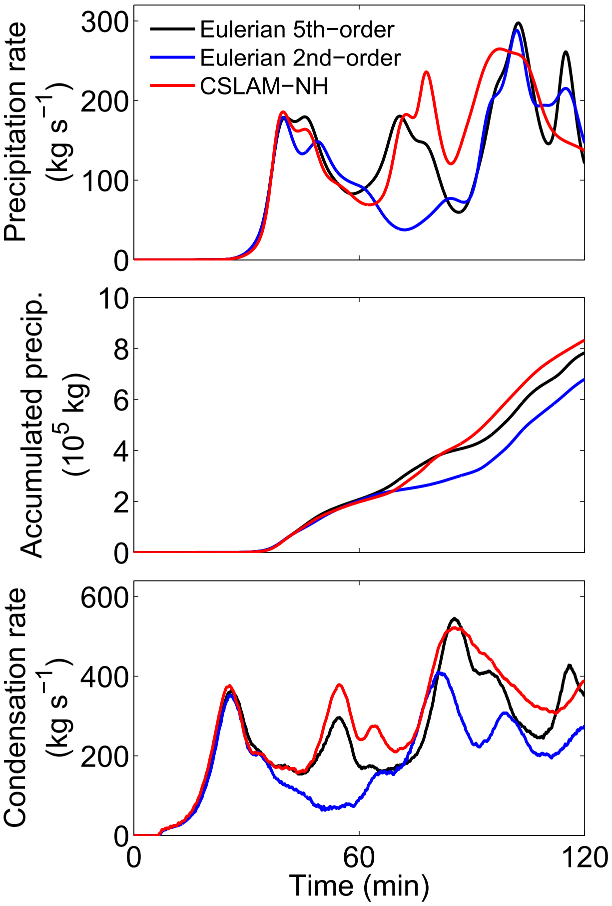

FIG. 9. Moisture statistics for (top) surface precipitation rate (kg s^{-1}), (middle) accumulated surface precipitation (kg), and (bottom) condensation rate (kg s^{-1}) from the microphysics using CSLAM-NH, Eulerian fifth-order horizontal advection, and Eulerian second-order horizontal advection at $\Delta x = \Delta z = 500$ m.

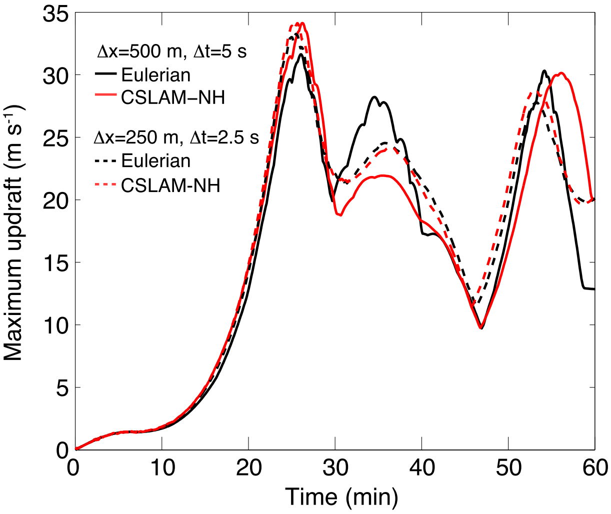

FIG. 10. Updraft intensities using CSLAM-NH (red) and Eulerian fifth-order horizontal advection (black) at $\Delta x = \Delta z = 500$ m and $\Delta t = 5$ s (solid), and $\Delta x = \Delta z = 250$ m and $\Delta t = 2.5$ s (dashed).

and enhanced uplift lead to the storm tilting in a near-upright position ($T = 0.8$ h). At 1.3 h, a new cell is triggered near the edge of the cold pool, where uplift of the warm moist air in the boundary layer is enhanced. At 1.7 h, the cold pool is strong enough to generate a circulation such that the system develops an upshear orientation, as described in Rotunno et al. (1988). Comparing to the simulations from the Eulerian second-order model, those from CSLAM-NH show closer resemblance to those from the Eulerian fifth-order model. The better agreement is also evident in the moisture statistics (Fig. 9), especially in the accumulated surface precipitation amounts and condensation rate in the domain.

Focusing on the two models that show more comparable results, the first maximum updraft velocities from CSLAM-NH (34.1 m s^{-1}) is slightly greater than that from Eulerian fifth-order advection (31.6 m s^{-1}) (Fig. 10). CSLAM-NH appears to show a weaker second peak updraft velocity (21.9 m s^{-1}) than the Eulerian fifth-order model (28.3 m s^{-1}); however, the stronger first peak (~34 m s^{-1}) and weaker second peak (~25 m s^{-1}) are also observed in a higher-resolution simulation using the Eulerian fifth-order model at a grid spacing of 250 m and large time step size of 2.5 s (dashed black line in Fig. 10). For comparison, maximum updraft from CSLAM-NH at $\Delta x = 250$ m and $\Delta t = 2.5$ s (red dashed line in Fig. 10) is also shown, and at the higher resolution, the two models agree very well with each other.

The maximum stable time step in the Eulerian split-explicit fifth-order advection scheme is a large time step of 20 s and acoustic time step size of 1.25 s. The maximum CSLAM-NH stable time step is limited to 15 s because of the violation of the Lipschitz stability condition in the vicinity of the updraft when a larger time step is used (the instability occurs when the storm reaches its first maximum vertical updraft, which generates a strong horizontal wind shear between the updraft and the neighboring downdraft). In Fig. 11, we see at larger time step sizes, maximum updraft velocities remain close to the small time-step solutions.

With the 2D squall-line test case, we examine the shape-preservation properties of CSLAM-NH using the shape-preserving scheme by Barth and Jespersen (1989) in the CSLAM transport scheme and the upwind scheme for the flux-correction terms in the transport equations. An analogous implementation of these schemes for a shallow-water model is described in Wong et al. (2013).

To verify that consistency is achieved, an additional passive tracer with mixing ratio r is introduced into the model. The passive tracer initially has a constant mixing ratio of $r_0 = 1.0$ g kg^{-1} and we form the discretized

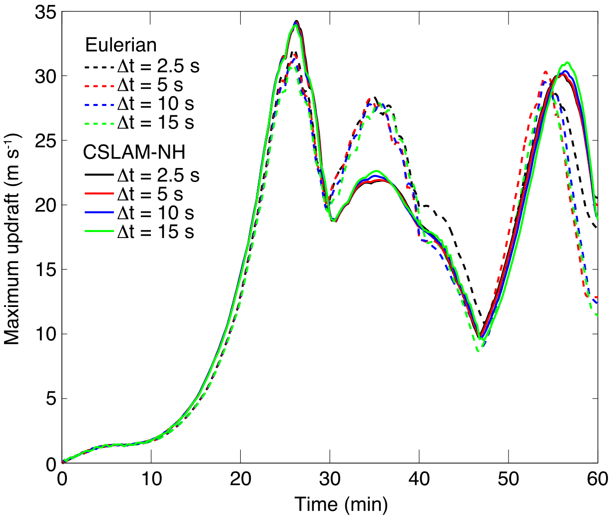

FIG. 11. Timing and intensity of the maximum vertical updraft using $\Delta x = \Delta z = 500$ m at different CSLAM-NH time step sizes (solid lines), as compared to the Eulerian fifth-order horizontal advection vertical velocity (dashed lines). (Only the first hour is plotted.)

conservation equation as in Eq. (23). The minimum and maximum values of r are maintained at 1.0 g kg^{-1} (up to machine round-off of order 10^{-14}) throughout the simulation using the consistent formulation in CSLAM-NH.

For a passive tracer that uses an inconsistent discrete conservation equation such as in Eq. (26), unphysical minima and maxima of the passive tracer mixing ratio are generated (Fig. 12). At the end of the squall line simulation at 2 h, the minimum and maximum mixing ratios r are 0.986 and 1.021 g kg^{-1}, respectively (i.e., the error is on the order of 1 part in 100). We note that the shape-preserving limiter described in Barth and Jespersen (1989) was also applied in CSLAM in this test. Because of numerical inconsistency, however, the limiter becomes ineffective agreeing with the results in Wong et al. (2013). This discrepancy from constancy highlights the importance of ensuring numerical consistency to properly maintain conservation of moisture and tracer mass in a semi-implicit CISL solver.

6. Summary

A new cell-integrated semi-Lagrangian (CISL) nonhydrostatic atmospheric solver, CSLAM-NH, for the moist Euler equations is introduced in this paper. The two-dimensional (x–z) Cartesian nonhydrostatic solver uses a CISL transport scheme, CSLAM, for conservative transport. It also incorporates a new approach to ensure numerical consistency among the CISL continuity

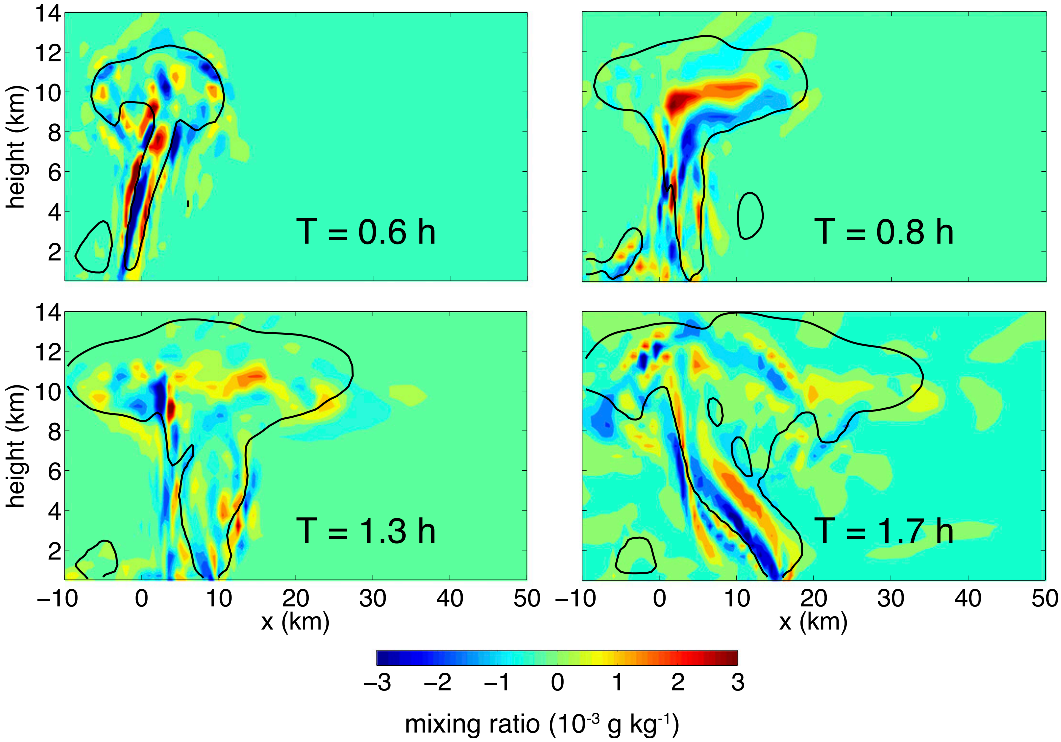

FIG. 12. Mixing ratio errors (g kg^{-1}) due to numerical inconsistency associated with Eq. (26) for times $T = 0.6$, 0.8, 1.3, and 1.7 h. The passive tracer is initialized with a uniform mixing ratio field of 1.0 g kg^{-1}. The consistent formulation in CSLAM-NH [which does not use Eq. (26)] ensures mixing ratio constancy of the same passive tracer up to machine round-off of order 10^{-14} (not shown).

equation and the conservation equations for potential temperature, moisture species, and passive tracers. A semi-implicit time integration scheme is used to stably handle the fast-moving acoustic waves in the compressible system.

Based on a recently tested shallow-water equations solver, the extended nonhydrostatic atmospheric solver presented here, CSLAM-NH, possesses a number of features ideal for weather and climate modeling purposes. The solver

1) is inherently mass conserving through the use of a conservative transport scheme CSLAM,
2) ensures numerical consistency between the continuity equation and other scalar mass conservation equations (the lack of which may lead to violation of scalar mass conservation),
3) does not depend on a mean reference state,
4) can be easily implemented with existing shape-preserving filters to ensure shape preservation of scalar fields,
5) requires a single linear Helmholtz equation solution (as in typical semi-implicit solvers) per time step, and
6) requires a single application of CSLAM per time step.

Here, we tested the nonhydrostatic extension for three idealized test cases: a density current, a gravity wave, and a squall line. To represent microphysical processes in the squall-line test, the Kessler warm-rain microphysics parameterization scheme is coupled to the dynamics. The 2D solver currently does not admit flow in the y direction, and therefore, Coriolis terms are neglected; however, the tests we present allow for sufficient testing of typical meteorological flows. Results compare well with other existing Eulerian (such as ARW-WRF) and nonhydrostatic CISL solvers (such as the nonhydrostatic SLICE model). In the density current and gravity wave tests, we see that CSLAM-NH allows for stable time steps 2 times larger than that in an Eulerian model. In the highly nonhydrostatic flow of the squall-line test case, the maximum stable time step size is of similar magnitude as the Eulerian split-explicit model. The strong wind shear across the storm updraft imposes a time step limit in CSLAM-NH due to the Lipschitz stability condition (violation of which leads to the crossing of trajectories).

Plans to extend the nonhydrostatic solver to include orographic influences are also under way. This work involves transformation of the nonhydrostatic equations into a terrain-following height coordinate. In traditional semi-Lagrangian semi-implicit solvers, flow over topography has been found to trigger spurious resonances and time off-centering in the implicit scheme has been found to eliminate these noises. Thus far, without orography, we have found that our nonhydrostatic solver only requires time off-centering ($\beta = 0.1$) in the squall-line case to maintain numerical stability. The nonhydrostatic solver with orography will allow us to test the conservative and consistent transport and stability of the new semi-implicit CISL discretization under the influence of a terrain-following coordinate.

Acknowledgments. This work was done as a part of the National Center for Atmospheric Research Graduate Visitor Advanced Study Program. The first author would also like to acknowledge the Canadian Natural Science and Engineering Research Council for their financial support via the Discovery Grant to the last author.

REFERENCES

Barth, T. J., and D. C. Jespersen, 1989: The design and application of upwind schemes on unstructured meshes. *Proc. 27th Aerospace Sciences Meeting,* Reno, NV, AIAA, AIAA-89-0366.

Erath, C., P. H. Lauritzen, J. H. Garcia, and H. M. Tufo, 2012: Integrating a scalable and efficient semi-Lagrangian multi-tracer transport scheme in HOMME. *Proc. Comput. Sci.,* **9,** 994–1003.

——, ——, and H. M. Tufo, 2013: On mass-conservation in high-order high-resolution rigorous remapping schemes on the sphere. *Mon. Wea. Rev.,* **141,** 2128–2133.

Harris, L. M., P. H. Lauritzen, and R. Mittal, 2011: A flux-form version of the conservative semi-Lagrangian multi-tracer transport scheme (CSLAM) on the cubed sphere grid. *J. Comput. Phys.,* **230,** 1215–1237.

Jablonowski, C., 2004: Adaptive grids in weather and climate modeling. Ph.D. thesis, University of Michigan, 292 pp.

Jöckel, P., R. von Kuhlmann, M. Lawrence, B. Steil, C. Brenninkmeijer, P. Crutzen, P. Rasch, and B. Eaton, 2001: On a fundamental problem in implementing flux-form advection schemes for tracer transport in 3-dimensional general circulation and chemistry transport models. *Quart. J. Roy. Meteor. Soc.,* **127,** 1035–1052.

Klemp, J. B., and R. B. Wilhelmson, 1978: The simulation of three-dimensional convective storm dynamics. *J. Atmos. Sci.,* **35,** 1070–1096.

——, W. C. Skamarock, and J. Dudhia, 2007: Conservative split-explicit time integration methods for the compressible nonhydrostatic equations. *Mon. Wea. Rev.,* **135,** 2897–2913.

Laprise, J., and A. Plante, 1995: A class of semi-Lagrangian integrated-mass (SLIM) numerical transport algorithms. *Mon. Wea. Rev.,* **123,** 553–565.

Lauritzen, P. H., E. Kaas, and B. Machenhauer, 2006: A mass-conservative semi-implicit semi-Lagrangian limited-area shallow-water model on the sphere. *Mon. Wea. Rev.,* **134,** 1205–1221.

——, ——, ——, and K. Lindberg, 2008: A mass-conservative version of the semi-implicit semi-Lagrangian HIRLAM. *Quart. J. Roy. Meteor. Soc.,* **134,** 1583–1595.

——, R. D. Nair, and P. A. Ullrich, 2010: A conservative semi-Lagrangian multi-tracer transport scheme (CSLAM) on the cubed-sphere grid. *J. Comput. Phys.,* **229,** 1401–1424.

——, W. C. Skamarock, M. J. Prather, and M. A. Taylor, 2012: A standard test case suite for two-dimensional linear transport on the sphere. *Geosci. Model Dev.,* **5,** 887–901.

——, and Coauthors, 2013: A standard test case suite for two-dimensional linear transport on the sphere: Results from a collection of state-of-the-art schemes. *Geosci. Model Dev. Discuss.,* **6** (3), 4983–5076.

Machenhauer, B., and M. Olk, 1997: The implementation of the semi-implicit scheme in cell-integrated semi-Lagrangian models. *Atmos.–Ocean,* **35** (Special Issue), 103–126.

——, E. Kaas, and P. H. Lauritzen, 2009: Finite volume meteorology. *Computational Methods for the Atmosphere and the Oceans: Special Volume,* R. Temam and J. Tribbia, Eds., Elsevier, 3–120.

McGregor, J. L., 1993: Economical determination of departure points for semi-Lagrangian models. *Mon. Wea. Rev.,* **121,** 221–230.

Melvin, T., M. Dubal, N. Wood, A. Staniforth, and M. Zerroukat, 2010: An inherently mass-conserving iterative semi-implicit semi-Lagrangian discretization of the non-hydrostatic vertical-slice equations. *Quart. J. Roy. Meteor. Soc.,* **136,** 799–814.

Nair, R. D., and B. Machenhauer, 2002: The mass-conservative cell-integrated semi-Lagrangian advection scheme on the sphere. *Mon. Wea. Rev.,* **130,** 649–667.

——, and P. H. Lauritzen, 2010: A class of deformational flow test cases for linear transport problems on the sphere. *J. Comput. Phys.,* **229,** 8868–8887.

Rancic, M., 1992: Semi-Lagrangian piecewise biparabolic scheme for two-dimensional horizontal advection of a passive scalar. *Mon. Wea. Rev.,* **120,** 1394–1406.

Rasch, P., and D. Williamson, 1990: Computational aspects of moisture transport in global-models of the atmosphere. *Quart. J. Roy. Meteor. Soc.,* **116,** 1071–1090.

Robert, A., 1981: A stable numerical integration scheme for the primitive meteorological equations. *Atmos.–Ocean,* **19,** 35–46.

——, T. Yee, and H. Ritchie, 1985: A semi-Lagrangian and semi-implicit numerical-integration scheme for multilevel atmospheric models. *Mon. Wea. Rev.,* **113,** 388–394.

Rotunno, R., J. B. Klemp, and M. L. Weisman, 1988: A theory for strong, long-lived squall lines. *J. Atmos. Sci.,* **45,** 463–485.

Skamarock, W. C., and J. B. Klemp, 1994: Efficiency and accuracy of the Klemp–Wilhelmson time-splitting technique. *Mon. Wea. Rev.,* **122,** 2623–2630.

——, and ——, 2008: A time-split nonhydrostatic atmospheric model for weather research and forecasting applications. *J. Comput. Phys.,* **227,** 3465–3485.

Straka, J., R. B. Wilhelmson, L. J. Wicker, J. R. Anderson, and K. K. Droegemeier, 1992: Numerical solutions of a non-linear density current: A benchmark solution and comparisons. *Int. J. Numer. Methods Fluids,* **17,** 1–22.

Ullrich, P. A., P. H. Lauritzen, and C. Jablonowski, 2012: Some considerations for high-order 'incremental remap'-based transport schemes: Edges, reconstructions, and area integration. *Int. J. Numer. Methods Fluids,* **71,** 1131–1151.

Weisman, M. L., and J. B. Klemp, 1982: The dependence of numerically simulated convective storms on vertical wind shear and buoyancy. *Mon. Wea. Rev.,* **110,** 504–520.

——, ——, and R. Rotunno, 1988: Structure and evolution of numerically simulated squall lines. *J. Atmos. Sci.,* **45,** 1990–2013.

Wong, M., W. C. Skamarock, P. H. Lauritzen, and R. B. Stull, 2013: A cell-integrated semi-Lagrangian semi-implicit shallow-water model (CSLAM-SW) with conservative and consistent transport. *Mon. Wea. Rev.,* **141,** 2545–2560.

Xue, M., K. K. Droegemeier, and V. Wong, 2000: The Advanced Regional Prediction System (ARPS)—A multi-scale non-hydrostatic atmospheric simulation and prediction model. Part I: Model dynamics and verification. *Meteor. Atmos. Phys.,* **75,** 161–193.

Zerroukat, M., N. Wood, and A. Staniforth, 2002: SLICE: A semi-Lagrangian inherently conserving and efficient scheme for transport problems. *Quart. J. Roy. Meteor. Soc.,* **128,** 2801–2820.

Zhang, K., H. Wan, B. Wang, and M. Zhang, 2008: Consistency problem with tracer advection in the atmospheric model GAMIL. *Adv. Atmos. Sci.,* **25,** 306–318.